A Numerical Study of Urban Aerosol Impacts on Clouds and Precipitation

JI-YOUNG HAN AND JONG-JIN BAIK

School of Earth and Environmental Sciences, Seoul National University, Seoul, South Korea

ALEXANDER P. KHAIN

Department of Atmospheric Sciences, The Hebrew University of Jerusalem, Jerusalem, Israel

(Manuscript received 24 February 2011, in final form 20 September 2011)

ABSTRACT

The impacts of urban aerosols on clouds and precipitation are investigated using a spectral (bin) microphysics cloud model. For this purpose, extensive numerical experiments with various aerosol concentrations are performed under different environmental moisture conditions. To take into account the urban heat island and urban air pollution, it is considered that there is low-level heating in the urban area and that the aerosol concentration in the urban area is higher than that in the surrounding rural area. Simulation results show that a low-level updraft induced by the urban heat island leads to the formation of a low-level cloud and then a deep convective cloud downwind of the urban area. The onset of precipitation produced by the low-level cloud is delayed at higher aerosol concentrations. This is because when the aerosol concentration is high, a narrow drop size distribution results in a suppressed collision–coalescence process and hence in late raindrop formation. However, after the deep convective cloud develops, a higher aerosol concentration generally leads to the development of a stronger convective cloud. This is mainly due to increased release of latent heat resulting from the enhanced condensation process with increasing aerosol concentration. The low collision efficiency of smaller cloud drops and the resulting stronger updraft at higher aerosol concentrations result in higher liquid water content at higher levels, leading to the enhanced riming process to produce large ice particles. The melting of a larger amount of hail leads to precipitation enhancement downwind of the urban area with increasing urban aerosol concentration in all moisture environments considered.

1. Introduction

It has been shown by many observational studies that more clouds, lightning, and precipitation occur over and downwind of urban areas (e.g., Changnon et al. 1991; Jauregui and Romales 1996; Orville et al. 2001; Shepherd et al. 2002; Inoue and Kimura 2004; Mote et al. 2007; Rose et al. 2008). Causes of urban-induced or urban-modified convective phenomena have been suggested, including the urban heat island, increased urban surface roughness, and increased urban aerosols (e.g., Baik et al. 2001; Shepherd 2005; van den Heever and Cotton 2007). Several observational (Bornstein and Lin 2000) and numerical (Baik et al. 2001; Rozoff et al. 2003) studies have indicated that the urban heat island plays an important role in initiating convective thunderstorms and resulting precipitation on the downwind side of urban areas, whereas upwind convergence induced by increased urban surface roughness is not strong enough to initiate moist convection. Previous studies on the role of aerosols in suppressing or enhancing convective activity are in debate (Shepherd 2005). Some studies have shown that anthropogenic air pollution can suppress precipitation because increased aerosol concentration results in many small cloud drops that coalesce inefficiently into raindrops (e.g., Rosenfeld 2000). On the other hand, some studies have found that the reduced cloud drop size, and therefore the delayed onset of precipitation, can allow invigoration of the updrafts, causing intense precipitation (e.g., Andreae et al. 2004).

Numerous observational studies have tried to demonstrate the relations between anthropogenic air pollution and urban-induced or urban-modified convective phenomena. By analyzing the relation between the weekly cycles of pollution and urban precipitation, Bell et al. (2008) and Lacke et al. (2009) found that larger

Corresponding author address: Jong-Jin Baik, School of Earth and Environmental Sciences, Seoul National University, Seoul 151-742, South Korea.
E-mail: jjbaik@snu.ac.kr

DOI: 10.1175/JAS-D-11-071.1

precipitation amounts occur on high aerosol concentration days. A positive correlation between the aerosol [e.g., particulate matter less than 10 μm in diameter (PM10)] concentration and the number of cloud-to-ground flashes over urban areas was also found by Westcott (1995), Naccarato et al. (2003), and Kar et al. (2009). However, it is difficult to decouple the effects of other environmental factors from those of aerosols in such observational studies. Many numerical studies have shown that the increase in aerosol concentration can inhibit or enhance convective activity depending on environmental conditions such as atmospheric humidity, instability, and vertical wind shear (e.g., Seifert and Beheng 2006; Khain et al. 2008; Lee et al. 2008; Khain 2009).

Many numerical studies have used bulk microphysics schemes to examine aerosol effects on clouds and precipitation. However, bulk microphysics schemes cannot take into account changes in the size distributions of hydrometeors. By performing simulations of a hailstorm using a two-moment bulk microphysics scheme with different prescribed cloud drop size distributions, Noppel et al. (2010) recently showed that the characteristics of the convective storm exhibit different responses to changes in aerosol concentration depending on the shape of the cloud drop size distribution. For example, the maximum amount of accumulated precipitation generally decreases with increasing aerosol concentration for a narrow distribution with many small droplets and for a broad distribution, but such a trend is not found for a narrow distribution with many large droplets. No clear dependence of hail amount and hail size on aerosol concentration was found in that study. On the other hand, simulations of the same hail storm using a cloud model with spectral (bin) microphysics indicated significant increases in hail precipitation and hail size with increasing aerosol concentration (Khain et al. 2011). Considering the limitation of the bulk schemes, it would be more appropriate to use a spectral microphysics scheme, which explicitly calculates changes in the size distributions of hydrometeors, for studying aerosol-induced changes in cloud microphysics.

This study examines how increased aerosol concentration in an urban area affects clouds and precipitation by using a spectral microphysics cloud model. Understanding the mechanisms of precipitation enhancement or suppression due to aerosols through real-case simulations is a difficult task because of the high degree of complexity (Ntelekos et al. 2009). In this study, we design a set of idealized experiments. Extensive numerical experiments are performed with various aerosol concentrations in different moisture environments. The urban heat island is specified with low-level heating, and urban air pollution is represented by a larger number of aerosols in the urban area. In this study, it will be shown that the amount of surface precipitation induced by an urban heat island changes significantly depending on the aerosol concentration in the urban area and that a higher aerosol concentration generally results in more precipitation downwind of the urban area. In section 2, the numerical model used in this study and the experimental design are described. In section 3, results of the numerical experiments are presented and discussed. Finally, a summary and conclusions are given in section 4.

2. Numerical model and experimental design

a. Numerical model

The numerical model used in this study is the Hebrew University Cloud Model (HUCM), which is a two-dimensional, nonhydrostatic, anelastic cloud model with spectral microphysics (Khain and Sednev 1996; Khain et al. 2004, 2005, 2008). The model solves kinetic equations for size distribution functions of one water and six ice hydrometeor types [water drops, three types of ice crystals (columns, plates, and dendrites), snowflakes, graupel, and hail], as well as atmospheric aerosol particles. Each size distribution function is represented by 43 mass-doubling bins. The size ranges of aerosol particles and hydrometers are 0.000 12–2 μm and 2 μm–3.3 cm, respectively. In this study, aerosol particles with radii smaller than 0.0031 μm are not considered and water drops with radii larger than 100 μm are assigned as raindrops. The microphysical processes included are the nucleation of droplets and ice crystals; diffusional growth/evaporation of drops; deposition/sublimation of ice particles; freezing of drops; drop–drop, drop–ice, and ice–ice collisions; sedimentation of particles; melting of ice particles; and breakup of drops. To take into account the effects of turbulence on the collision process, the collision enhancement factors are multiplied on the collision kernels following Pinsky and Khain (1998) and Pinsky et al. (1999, 2000).

When supersaturation occurs, activated cloud condensation nuclei (CCN) particles with radii larger than $r_{N\mathrm{crit}}$ are formed. Here, $r_{N\mathrm{crit}}$ is the minimum radius of activated CCN particles and is calculated according to the Köhler theory (Köhler 1936; Pruppacher and Klett 1997):

$$r_{N\mathrm{crit}} = \frac{A}{3}\left(\frac{4}{BS^2}\right)^{1/3}, \tag{1}$$

where

$$A = \frac{2\sigma_{w/a}}{R_v T \rho_w}, \quad B = \frac{3\nu m_s M_w}{4\pi M_s \rho_w}.$$

Here, $\sigma_{w/a}$ is the surface tension for a water–humid air interface, R_v is the specific gas constant for water vapor,

TABLE 1. Thermodynamic parameters of the soundings considered in this study. The mixing ratio in the lowest 1 km (q_L), relative humidity averaged over the lowest 1 km (RH_L), maximum relative humidity (RH_{max}), convective available potential energy (CAPE), convective inhibition (CIN), lifting condensation level (LCL), and level of neutral buoyancy (LNB) are given.

q_L (g kg^{-1})	RH_L (RH_{max}) (%)	CAPE (J kg^{-1})	CIN (J kg^{-1})	LCL (km)	LNB (km)
16	60 (69)	360	−210	1.4	9.8
17	64 (73)	630	−170	1.3	10.6
18	67 (77)	950	−140	1.1	11.3
19	71 (82)	1310	−110	1.0	11.9
20	75 (86)	1700	−90	0.9	12.4

T is the air temperature, ρ_w is the density of water, ν is the number of ions into which an aerosol molecule dissociates in water, m_s is the mass of aerosol, M_w and M_s are the molecular weights of water and aerosol, respectively, and S is the supersaturation with respect to water (%). Equation (1) shows that as S increases, smaller aerosol particles can be activated. Aerosol particles with $r_N \leq 0.4$ μm and $0.4 < r_N \leq 2$ μm are activated to cloud drops with $r = 2$ μm (i.e., minimum radius of cloud drops) and $r = 5r_N$, respectively (i.e., the maximum radius of nucleated cloud drops is 10 μm). Here, r_N and r are the radii of aerosol particles and cloud drops, respectively.

b. Experimental design

The basic-state temperature decreases linearly with a constant lapse rate of 6.5 K km^{-1} from the surface to $z = 16$ km and is constant above that height. The basic-state temperature at the surface is specified as 305.15 K. For this temperature profile, the freezing level and the level where homogeneous freezing starts to occur ($T = 235.15$ K) are about $z = 4.9$ and 10.8 km, respectively. The basic-state mixing ratio is constant from the surface to $z = 1$ km with a value of q_L, decreases exponentially with an e-folding depth of 2 km up to $z = 11$ km, and is set to a value that makes the relative humidity remain constant above that height. In this study, various moisture profiles are considered because some numerical studies have shown that the degree of atmospheric humidity can change the dependence of convective activity on aerosol concentration (e.g., Lynn et al. 2007; Tao et al. 2007; Khain et al. 2008). The basic-state mixing ratio in the lowest 1 km (q_L) is specified as 16, 17, 18, 19, and 20 g kg^{-1}. The thermodynamic parameters corresponding to each moisture profile are given in Table 1. The corresponding relative humidity averaged over the lowest 1 km (RH_L) and maximum relative humidity (RH_{max}) change from 60% to 75% and from 69% to 86%, respectively. In all cases, the lifting condensation level (LCL) is lower than the freezing level and hence clouds with warm cloud base are produced. The basic-state horizontal wind is assumed to be constant with height with a value of 3 m s^{-1}. This rather small value is chosen to take into account the fact that the urban heat island is well established under weak winds (e.g., Oke 1987).

The diabatic forcing q, which is considered to represent an urban heat island, is bell-shaped in the horizontal and decreases exponentially in the vertical:

$$q(x,z,t) = \frac{q_0 f(t)}{c_p} \frac{a_x^2}{(x-c)^2 + a_x^2} e^{-z/h}, \tag{2}$$

where

$$f(t) = \begin{cases} 1 & \text{for} \quad 0 \leq t \leq t_{\text{rain}} \\ 1 - \dfrac{t - t_{\text{rain}}}{\tau} & \text{for} \quad t_{\text{rain}} < t \leq t_{\text{rain}} + \tau \\ 0 & \text{for} \quad t > t_{\text{rain}} + \tau \end{cases}.$$

Here, q_0 is the amplitude of the diabatic forcing, c_p is the specific heat of air at constant pressure, a_x is the half-width of the bell-shaped function, c is the horizontal location of the center of the urban heat island, h is the e-folding heating depth, and t_{rain} is the initiation time of surface precipitation. To take into account the fact that rainy weather conditions weaken the urban heat island or make it disappear (e.g., Oke 1987), the amplitude of the diabatic forcing is specified to decrease linearly with time after the initiation of surface precipitation and become zero some time τ after the onset of surface precipitation. In all numerical experiments, $q_0 = 0.6$ J kg^{-1} s^{-1}, $a_x = 10$ km, $c = 50$ km, $h = 350$ m, and $\tau = 30$ min.

For each moisture profile, nine different kinds of initial spatial distribution of CCN concentration are considered ($n = 1, 2, \ldots, 9$):

$$N(n) = N_0(n) S^k, \tag{3}$$

where

$$N_0(n) = N_1 f_n(x) g(z),$$

$$f_1(x) = 1,$$

$$f_n(x) = \begin{cases} 1 & \text{for} \quad |x-c| \geq 1.5a_x \\ \dfrac{a_n^2}{(x-c)^2 + a_n^2} 2^{n-1} & \text{for} \quad |x-c| < 1.5a_x \end{cases}$$

if $n \neq 1$,

$$a_n = \frac{1.5a_x}{\sqrt{2^{n-1} - 1}} \quad \text{if} \quad n \neq 1,$$

$$g(z) = \begin{cases} 1 & \text{for} \quad 0 \leq z \leq h_1 \\ \exp[-(z - h_1)/h_2] & \text{for} \quad z > h_1 \end{cases}.$$

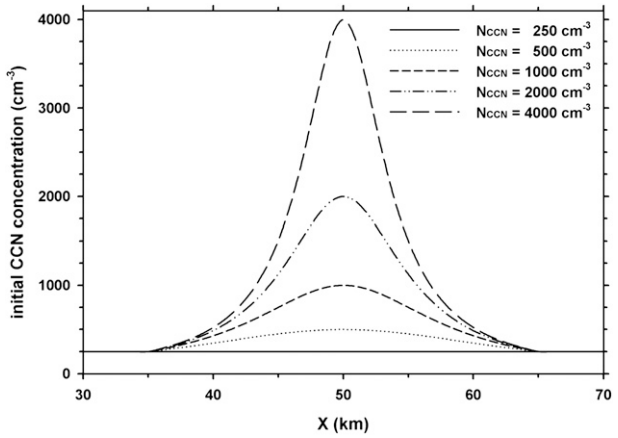

FIG. 1. The initial spatial distributions of CCN concentration at 1% supersaturation in the lowest 1 km in the cases of N_{CCN} = 250, 500, 1000, 2000, and 4000 cm^{-3}.

Here, $N_1 = 250$ cm^{-3}, $h_1 = 1$ km, $h_2 = 2$ km, and $k = 0.5$. The first ($n = 1$) initial spatial distribution of CCN concentration is horizontally homogeneous in both rural and urban areas with a value of 250 cm^{-3} at 1% supersaturation in the lowest 1 km (solid line in Fig. 1). On the other hand, the other eight ($n = 2, 3, \ldots, 9$) spatial distributions of CCN concentration are specified to be horizontally inhomogeneous. The CCN concentration in the urban area ($|x - c| < 1.5a_x$) has a bell-shaped distribution with a maximum value at the urban center (Fig. 1). We determine a_n such that the CCN concentration at the boundaries of the urban area ($x = c \pm 1.5a_x$) is the same as that in the surrounding rural area ($|x - c| > 1.5a_x$), where the CCN concentration is horizontally homogeneous with a value of 250 cm^{-3}. The maximum CCN concentration, which is observed at the center of the urban area, at 1% supersaturation in the lowest 1 km is denoted by N_{CCN} ($=N_1 2^{n-1}$) and is specified as 500, 1000, 2000, 4000, 8000, 16 000, 32 000, and 64 000 cm^{-3}. Note that CCN concentrations higher than 16 000 cm^{-3} are beyond the observed value (e.g., Andreae 2009). However, these are included to examine the patterns of aerosol impacts in the range beyond the observed value and extreme cases that might occur in the future with much higher levels of urban air pollution. As time progresses, horizontal advection by basic-state wind and circulation induced by the urban heat island make the CCN concentration in inhomogeneous cases be relatively high not only in the urban area but also over a wide area downwind of the urban area (not shown). In all cases, the initial CCN concentration is constant from the surface to $z = 1$ km and decreases exponentially with an *e*-folding depth of 2 km above that height. The zero-gradient lateral boundary condition is imposed on CCN concentration.

TABLE 2. The time and the horizontal and vertical locations of the first cloud drop formation and the magnitude of the vertical velocity w where the first cloud drop is produced. Note that the urban center is located at $x = 50$ km.

q_L (g kg^{-1})	Time (min)	Horizontal location (km)	Vertical location (km)	w (m s^{-1})
16	200	59.00	2.000	0.48
17	183	58.25	1.875	0.39
18	167	57.75	1.750	0.33
19	152	57.25	1.625	0.28
20	138	56.50	1.500	0.24

The computational domain size is 256 km in the horizontal and 18 km in the vertical. A damping layer is included from $z = 14$ km to the model top height to minimize reflected gravity waves from the model top. The horizontal and vertical grid intervals are 250 and 125 m, respectively. The model is integrated up to $t = 6$ h with a time step of 4 s.

3. Results and discussion

Extensive experiments with various CCN concentrations and basic-state moisture profiles are performed to examine urban aerosol impacts on clouds and precipitation under different environmental conditions. To simplify explanations, the case of $N_{CCN} = 4000$ cm^{-3} and $q_L = 18$ g kg^{-1} is chosen as a control case and is compared with the case of $N_{CCN} = 500$ cm^{-3} and $q_L = 18$ g kg^{-1} when necessary. The former and the latter are called high and low CCN concentration cases, respectively.

The urban heat island induces a well-organized low-level updraft downwind of the urban center, as shown by previous studies (Baik et al. 2001, 2007; Han and Baik 2008). The first cloud drop is formed by the nucleation process when supersaturation occurs through adiabatic cooling in the upper part of the low-level updraft region. Table 2 shows the time and the horizontal and vertical locations of the first cloud drop formation and the magnitude of the vertical velocity where the first cloud drop is produced. The first cloud drop is produced later in drier environments because a stronger updraft is required for supersaturation as the atmosphere becomes drier. The magnitude of the vertical velocity where the first cloud drop is produced in the case of $q_L = 16$ g kg^{-1} is twice that in the case of $q_L = 20$ g kg^{-1}. In drier environments, the location of the first cloud drop formation is slightly farther downwind and at a slightly higher altitude. Note that the time and location of the first cloud drop formation and the magnitude of the vertical velocity where the first cloud drop is produced do not change with CCN concentration.

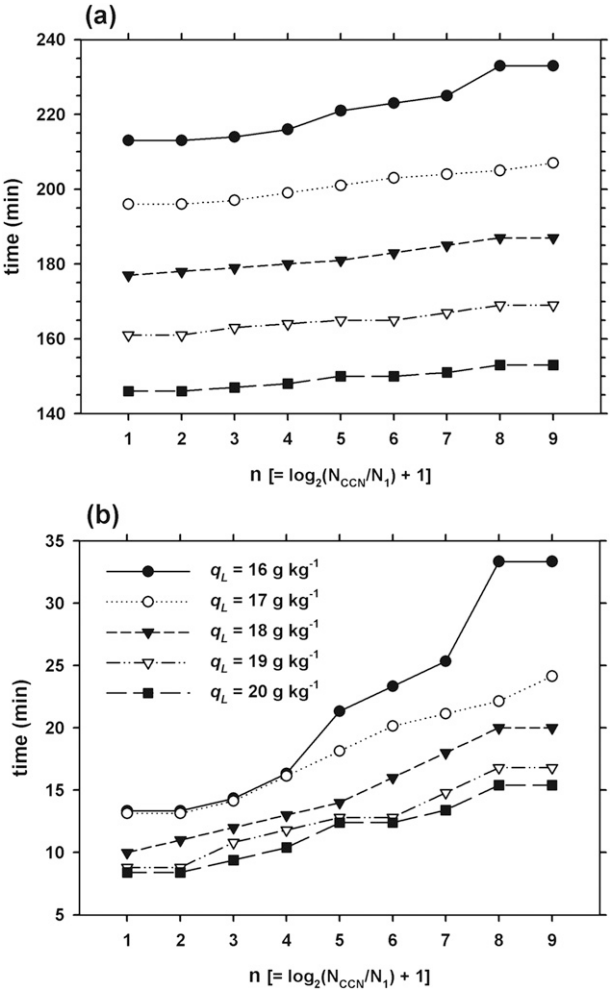

FIG. 2. (a) The time of the first raindrop formation and (b) the time required from the first cloud drop formation to the first raindrop formation $T_{C\rightarrow R}$ as a function of n (i.e., CCN concentration in the urban area) in the cases of q_L = 16, 17, 18, 19, and 20 g kg^{-1}. Note that $n = \log_2(N_{CCN}/N_1) + 1$.

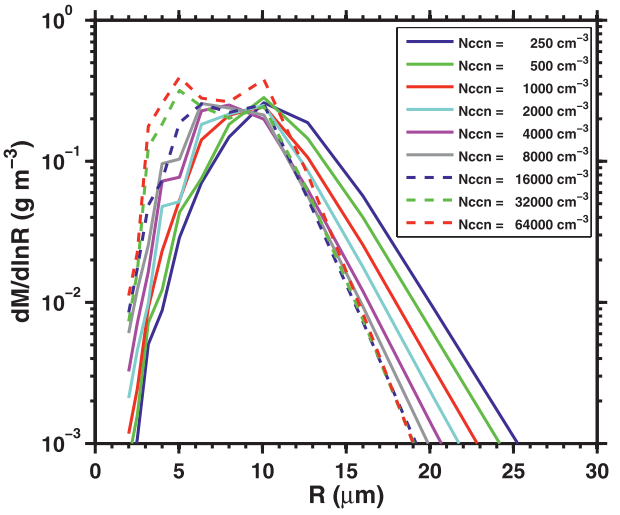

FIG. 3. The cloud drop size distributions (mass distributions) where the maximum cloud water content appears at t = 176 min (just prior to the first raindrop formation) with various CCN concentrations for q_L = 18 g kg^{-1}.

Nucleated cloud drops grow by diffusional growth and collision–coalescence between cloud drops, and hence raindrops are produced some time after cloud drop formation. A low-level cloud develops on the downwind side not far from the urban center. The time of the first raindrop formation and the time required from the first cloud drop formation to the first raindrop formation $T_{C\rightarrow R}$ in the low-level cloud differ for each CCN concentration in the urban area. This is shown in Fig. 2 for different environmental moisture conditions. For a given CCN concentration, the first raindrop formation occurs earlier and $T_{C\rightarrow R}$ becomes shorter in more humid environments, where the diffusional growth of cloud drops is enhanced by a larger amount of water vapor. For a given basic-state moisture profile, the first raindrop is generally formed later with increasing CCN concentration. This can be explained by Fig. 3, which depicts cloud drop size distributions where the maximum cloud water content appears at t = 176 min (just prior to the first raindrop formation) with various CCN concentrations for q_L = 18 g kg^{-1}. A higher CCN concentration results in the generation of a larger number of nucleated cloud drops, leading to decreased supersaturation. This slows down the diffusional growth of cloud drops, leading to a narrow drop size distribution that is inefficient in the collision–coalescence process. As a result, it generally takes longer to produce the first raindrop with increasing CCN concentration. Figure 2 also shows that for a given basic-state moisture profile, the increasing trends of both the time of the first raindrop formation and $T_{C\rightarrow R}$ with increasing CCN concentration are more marked at lower CCN concentrations than at higher CCN concentrations [note that $n = \log_2(N_{CCN}/N_1) + 1$; i.e., N_{CCN} considered in this study increases exponentially, in proportion to 2^n]. In more humid environments, $T_{C\rightarrow R}$ is less sensitive to changes in CCN concentration. A higher CCN concentration increases the sensitivity of $T_{C\rightarrow R}$ to the basic-state moisture content.

Within the region of downward motion located right downwind of the low-level updraft, a well-organized low-level downdraft develops rapidly after the formation of the low-level cloud. The intensity of the low-level updraft induced directly by the urban heat island is nearly identical, regardless of the CCN concentration in the urban area. However, the intensity of the low-level downdraft that begins to develop rapidly after the formation of the

low-level cloud is stronger in the high CCN concentration case, as shown in Fig. 4a. An overall increasing trend of the intensity of the low-level downdraft with increasing CCN concentration is observed under all environmental moisture conditions considered (not shown). The reason for this can be explained by Figs. 4b–d, which compare the evaporative cooling rate, water vapor mixing ratio, and liquid water content fields of the low-level cloud in the low CCN concentration case (left column) with the corresponding fields in the high CCN concentration case (right column) near the time of the maximum intensity of the low-level downdraft (i.e., at $t = 220$ min). Figure 4b indicates that a stronger low-level downdraft in the high CCN concentration case is mainly due to increased cooling in the downdraft region that results from enhanced evaporation of cloud drops. In addition, the increased vertical advection of dry air due to a stronger downdraft also results in a further increase in downdraft intensity by reducing water vapor buoyancy (Fig. 4c). On the other hand, the hydrometeor drag (hydrometeor loading) effect, which is included in the vertical momentum equation as a term of $-gq_H$ (where q_H is the total hydrometeor mixing ratio), is stronger in the low CCN concentration case, in which a larger amount of rainwater exists in the downdraft region (Fig. 4d), but this effect is not significant.

Figure 5a shows the drop size distributions averaged over the area where the number concentration of water drops is larger than 1 cm^{-3} at $t = 220$ min with various CCN concentrations for $q_L = 18$ g kg^{-1}. Two local peaks are observed in the drop size distribution: one is for cloud drops and the other is for raindrops. The cloud drop size distribution tends to shift to a smaller drop size and its maximum increases with increasing CCN concentration. On the other hand, the raindrop size distribution, whose magnitude is much smaller than that of the cloud drop size distribution, shows no shift and its maximum decreases with increasing CCN concentration. Both the smaller drop size and the increased liquid mass available for evaporation result in an increase in evaporative cooling rate with increasing CCN concentration, as shown in Fig. 5b. Note that the evaporative cooling rate below about $z = 1.6$ km, where its value is small, increases with decreasing CCN concentration. This is because evaporative cooling in this layer is caused by the evaporation of raindrops whose content increases with decreasing CCN concentration (Fig. 5a).

The low-level cloud produces surface precipitation downwind of the urban center, but the precipitation amount is very small. Figure 6 shows the initiation time of surface precipitation produced by the low-level cloud and the time required from the first raindrop formation to the initiation of surface precipitation $T_{R\rightarrow P}$ as a function of CCN concentration. For a given CCN concentration, as the environment becomes more humid, less time is required to initiate surface precipitation and $T_{R\rightarrow P}$ becomes shorter. For a given basic-state moisture content, it generally takes longer to initiate surface precipitation with increasing CCN concentration. This is due to the late formation of raindrops at higher CCN concentrations (see Fig. 2), even though $T_{R\rightarrow P}$ shows no clear relationship with CCN concentration (Fig. 6b). Surface precipitation is more likely to occur when large raindrops with high terminal fall speeds fall in the strong downdraft region. Because a higher CCN concentration results not only in a smaller amount of large raindrops but also in a stronger downdraft by enhancing evaporative cooling, the increase in CCN concentration does not necessarily delay $T_{R\rightarrow P}$.

Figure 7 shows the time evolution of the surface precipitation rate averaged over the surface precipitation area with various CCN concentrations for $q_L = 18$ g kg^{-1}. When the CCN concentration is high, the late formation of larger drops leads to the suppression of surface precipitation produced by the low-level cloud. However, this trend is reversed after the development of a deep convective cloud (after about $t = 233$ min in Fig. 7). This will be explained below.

After the low-level cloud produces surface precipitation, a weak updraft cell is separated from the upper-right part of the low-level updraft and induces convection that develops rapidly to become a deep convective cloud on the downwind side of the low-level cloud. The different CCN concentrations lead to changes in the intensity of the deep convective cloud. Figure 8 compares the vertical velocity, condensational heating rate, and liquid water content fields of the deep convective cloud in the low CCN concentration case (left column) with the corresponding fields in the high CCN concentration case (right column) at $t = 240$ min (before ice microphysical processes become active). A larger amount of latent heat is released up to higher levels in the high CCN concentration case through the enhanced diffusional growth process of cloud drops (Fig. 8b), causing stronger updraft and increased cloud-top height of the deep convective cloud (Fig. 8a). On the other hand, the hydrometeor drag effect, which acts to decrease updraft intensity, is stronger in the high CCN concentration case (Fig. 8c) because of not only a significant number of smaller cloud drops but also a large number of very large raindrops, as will be shown in Fig. 9a. However, this effect is negligible compared to the effect of condensational heating. The stronger updraft in the high CCN concentration case leads to stronger compensating downdraft and enhanced low-level convergence, but this is not strong enough to allow the formation of secondary clouds as in the low CCN

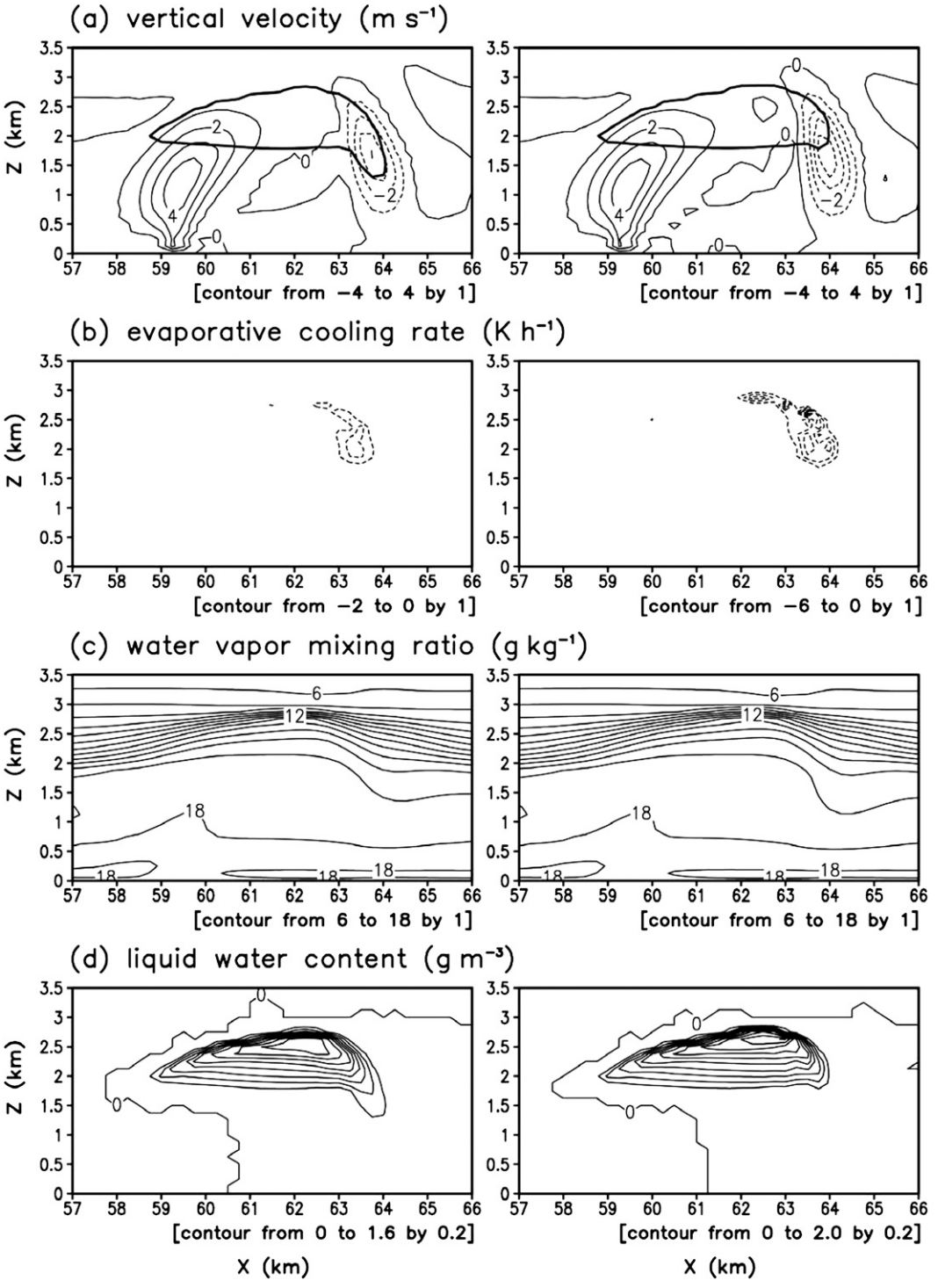

FIG. 4. The (a) vertical velocity, (b) evaporative cooling rate, (c) water vapor mixing ratio, and (d) liquid water content (LWC) fields near the time of the maximum intensity of the low-level downdraft (i.e., at $t = 220$ min) in the cases of $q_L = 18$ g kg^{-1} and N_{CCN} = (left) 500 and (right) 4000 cm^{-3}. Note that 0.1 g m^{-3} contour line of the LWC is also plotted by a thick solid line in (a). The urban center is located at $x = 50$ km.

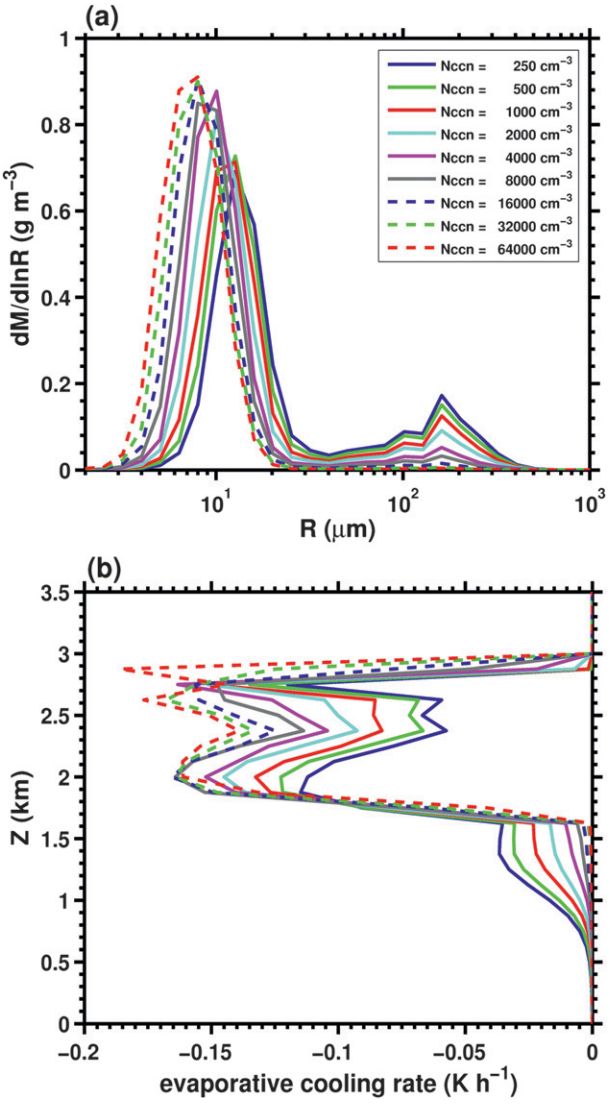

FIG. 5. (a) The drop size distributions averaged over the area where the number concentration of water drops is larger than 1 cm^{-3} and (b) the vertical profiles of evaporative cooling rate averaged over the domain at $t = 220$ min with various CCN concentrations for $q_L = 18$ g kg^{-1}.

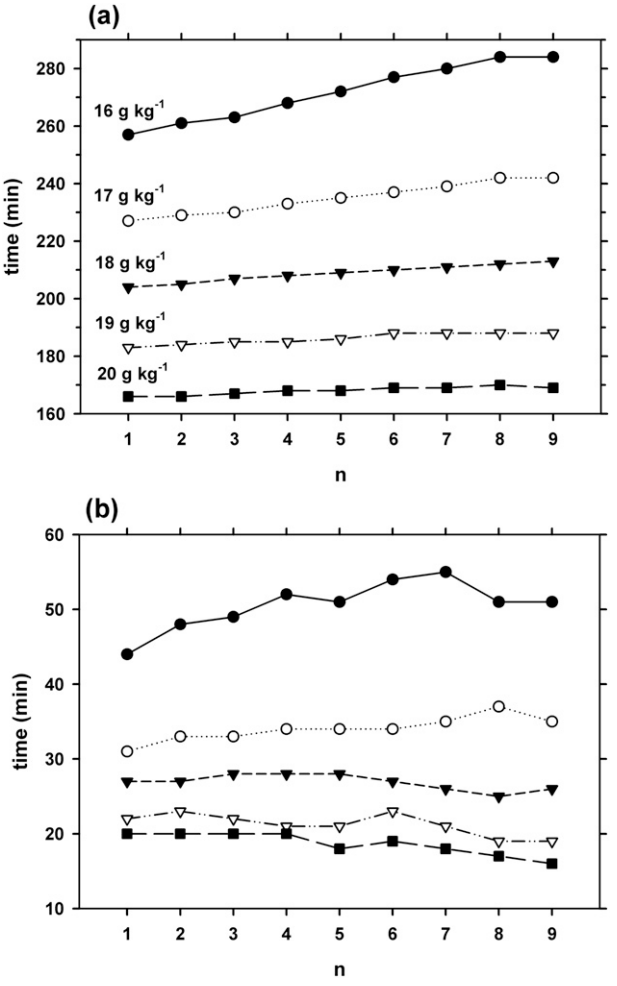

FIG. 6. (a) The initiation time of surface precipitation produced by the low-level cloud t_{rain} and (b) the time required from the first raindrop formation to the initiation of surface precipitation $T_{\text{R}\rightarrow\text{P}}$ as a function of n in the cases of $q_L = 16$, 17, 18, 19, and 20 g kg^{-1}.

concentration case. The formation and intensification of secondary clouds have been suggested as one mechanism causing precipitation enhancement at higher CCN concentrations for a mesoscale convective system (e.g., Khain et al. 2008; Lee et al. 2008; Khain 2009). Note that aerosol effects on clouds and precipitation and the mechanism involved are highly dependent on the cloud type.

Figure 9a shows the drop size distributions averaged over the area where supersaturation occurs within the deep convective cloud at $t = 240$ min. The cloud drop size distribution shifts to a smaller drop size and its maximum increases with increasing CCN concentration. Because smaller cloud drops have low collision efficiency and can therefore grow through the diffusional growth process up to higher levels with inactive collision with other drops, a larger amount of latent heat of condensation is released up to higher levels in the strong updraft region with increasing CCN concentration, as shown in Fig. 9b. This leads to stronger updraft and increased cloud-top height of the deep convective cloud at higher CCN concentrations as explained above. Note that the raindrop size distribution shows a tendency to shift to a larger drop size with increasing CCN concentration, producing a larger number of very large raindrops within the deep convective cloud. This causes the enhancement of surface precipitation produced by the warm rain process in the deep convective cloud (see Fig. 7). It takes longer time for raindrops to form and grow at higher CCN concentration

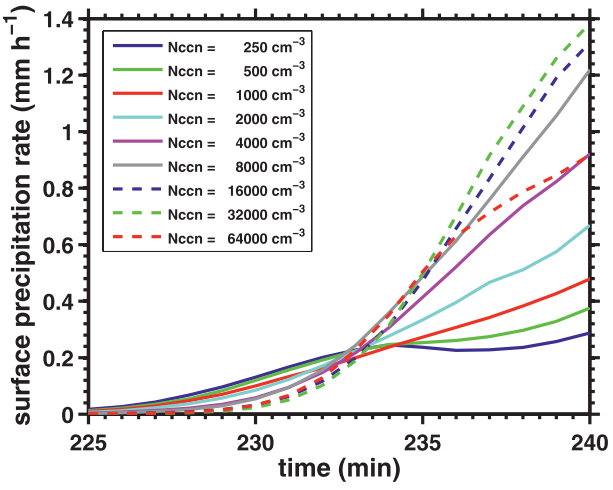

FIG. 7. The time evolution of the surface precipitation rate averaged over the surface precipitation area from $t = 225$ to 240 min with various CCN concentrations for $q_L = 18$ g kg^{-1}.

because of the suppressed collision–coalescence process resulting from a narrow drop size distribution (see Figs. 2, 3, and 5a). However, once large raindrops with high collision rates are produced, they can grow efficiently to larger sizes in the presence of high concentration of drops (Fig. 9b) because of an increased chance to collide with other drops, even though the sizes of other drops are very small.

The cloud-top height of the low-level cloud is lower than the freezing level, and hence only warm microphysical processes occur within the cloud. However, in the deep convective cloud that extends above the freezing level, both warm and ice microphysical processes become active. Next, we investigate how increased CCN concentration in the urban area affects ice microphysical processes in the deep convective cloud. Figure 10 compares the cloud water, ice crystal, snow, and hail content fields above $z = 5$ km in the low CCN concentration case (left column) with those in the high CCN concentration case (right column) near the time of maximum updraft in the deep convective cloud (i.e., at $t = 250$ min). High cloud water content exists up to higher levels in the high CCN concentration case (Fig. 10a). This is not only because, as mentioned above, a large number of smaller cloud drops with low collision efficiency can grow through the condensation process up to higher levels with inactive collision with other hydrometeors, but also because there is a stronger updraft in the deep convective cloud when the CCN concentration is high. As a result, the riming process, particularly the collisions of ice crystal and snow with supercooled drops to produce graupel/hail, is enhanced at higher levels in the high CCN concentration case. This is shown in Figs. 10b–d, where a much smaller amount of ice crystals and snow but a much larger amount of hail is observed at higher levels in the high CCN concentration case.

Figure 11 compares the vertical velocity field and the condensational, riming, and depositional heating rate fields in the low CCN concentration case (left column) with those in the high CCN concentration case (right column) at $t = 250$ min. Figures 11b and 11c also show that after ice microphysical processes become active, a larger amount of latent heat is released at higher altitudes (above $z = 8$ km) not only through the condensation process of supercooled cloud drops but also through the riming process of ice particles when the CCN concentration is high. On the other hand, lower supersaturation with respect to ice results in the suppression of the deposition process of ice particles in the high CCN concentration case (Fig. 11d).

Figure 12 shows the maximum intensity of the updraft and the corresponding local maximum precipitation rate of the deep convective cloud as a function of CCN concentration for $q_L = 18$ g kg^{-1}. The difference in the maximum intensity of the updraft between the low and high CCN concentration cases shows a slightly decreasing trend after the deposition process becomes active (not shown) because a much smaller amount of latent heat of deposition is released in the high CCN concentration case (Fig. 11d). However, the maximum updraft is still much stronger at higher CCN concentrations (Figs. 11a and 12a) because of the enhanced condensation process, causing an increase in cloud-top height. This cloud invigoration with increasing CCN concentration is consistent with the observational findings of Koren et al. (2005) and Lin et al. (2006). By analyzing satellite data over the northern Atlantic Ocean and the Amazon Basin, respectively, they showed that the cloud-top pressure decreases with increasing aerosol optical depth. The invigoration of the deep convective cloud generally leads to a higher local maximum precipitation rate near the time of maximum updraft with increasing CCN concentration (Figs. 12b,c). However, these increasing trends of the maximum intensity of the updraft and the corresponding local maximum precipitation rate do not appear at very high CCN concentrations.

After the occurrence of the precipitation event near the time of maximum updraft, the well-organized structure of the deep convective cloud is destroyed, producing several convective cells. The resulting cloud system produces a large amount of surface precipitation on the downwind side of the urban area through the ice-melting process. Figure 13 shows the time evolution of the melting rate with various CCN concentrations for $q_L = 18$ g kg^{-1}. After the precipitation event near the time of maximum updraft occurs, the melting rate increases dramatically

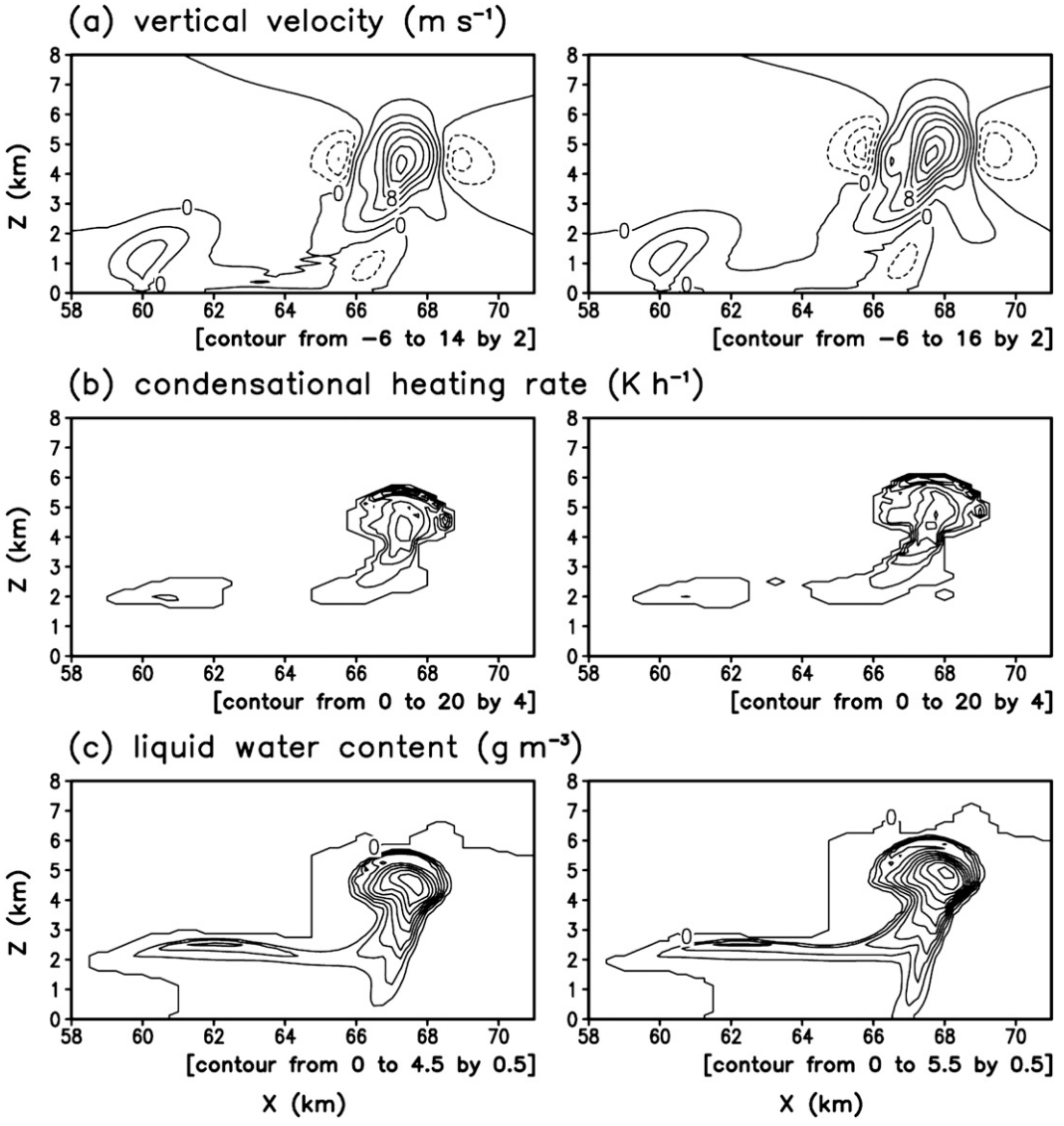

FIG. 8. The (a) vertical velocity, (b) condensational heating rate, and (c) LWC fields at $t = 240$ min (before ice microphysical processes become active) in the cases of $q_L = 18$ g kg^{-1} and N_{CCN} = (left) 500 and (right) 4000 cm^{-3}. The urban center is located at $x = 50$ km.

with increasing CCN concentration at relatively low and moderate CCN concentrations because of the melting of a larger amount of hail produced by the enhanced riming process. For relatively high CCN concentrations higher than 8000 cm^{-3} (dashed lines in Fig. 13), the increasing trend of the melting rate with increasing CCN concentration is relatively weak in the main precipitation period (from about $t = 257$ to 272 min), but another local peak appears after $t = 272$ min unlike at relatively low and moderate CCN concentrations. This occurs because at relatively high CCN concentrations, one of the convective cells redevelops into a more organized convective cloud, leading to the additional production of hail at a later time.

Figure 14 shows the time evolution and horizontal distribution of surface precipitation amount with various CCN concentrations. The melting of a larger amount of hail at higher CCN concentrations leads to a significant increase in the amount of surface precipitation produced by the deep convective cloud system. In particular, for relatively high CCN concentrations higher than 8000 cm^{-3}, high precipitation continues for a longer time (dashed lines in Fig. 14a). These results agree well with those reported recently by Khain et al. (2011) indicating that an increase in aerosol concentration leads to an increase in hail amount and accordingly to an increase in surface precipitation (since melted hail contributes significantly to surface

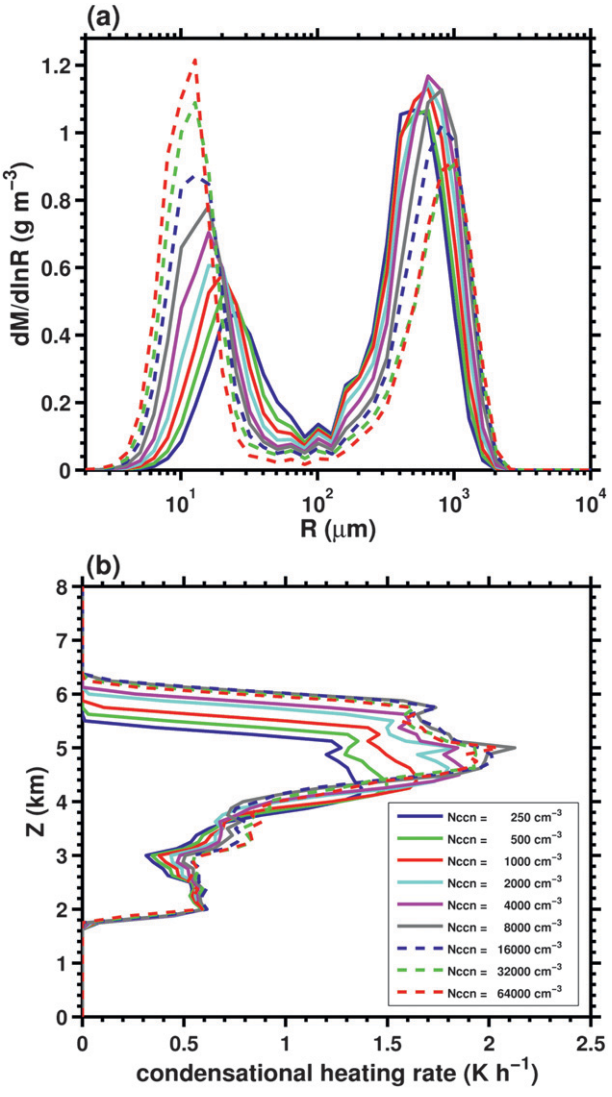

FIG. 9. (a) The drop size distributions averaged over the area where supersaturation occurs within the deep convective cloud and (b) the vertical profiles of condensational heating rate averaged over the domain at $t = 240$ min with various CCN concentrations for $q_L = 18$ g kg^{-1}.

precipitation). A dramatic change in the amount of surface precipitation with CCN concentration occurs on the downwind side more than 20 km away from the urban center (Fig. 14b). As the CCN concentration increases, the high precipitation region is observed farther downwind of the urban area.

Figure 15 shows the accumulated surface precipitation amount averaged over the domain as a function of CCN concentration under various environmental moisture conditions. For a given CCN concentration, the increase in the basic-state moisture content increases the accumulated surface precipitation amount except for the case of $q_L = 16$ g kg^{-1}, in which the convective system exhibits a different evolution. For basic-state moisture profiles where q_L is larger than 16 g kg^{-1}, a well-organized deep convective cloud develops, as shown in Fig. 11a using the case of $q_L = 18$ g kg^{-1} as an example. However, for $q_L = 16$ g kg^{-1}, some convective cells with a relatively shallow depth are produced within the convective cloud system, instead of a well-organized deep convective cloud (not shown). In this case, for relatively high CCN concentrations higher than 8000 cm^{-3} (i.e., for $n > 6$), one of the convective cells develops into a more organized deep convective cloud at a later time, resulting in a larger amount of surface precipitation than that in the corresponding case of $q_L = 17$ g kg^{-1}. For a given basic-state moisture profile, the accumulated surface precipitation amount shows an overall increasing trend with increasing CCN concentration, even though this trend is relatively weak for $q_L = 16$ g kg^{-1} and $n \leq 6$.

In our idealized experiments, the chemical composition of aerosol particles is assumed to be sea salt, even though urban areas are considered. To examine the sensitivity of our simulation results to the chemical composition of aerosol particles, numerical experiments were performed in which different chemical compositions of aerosol particles (ammonium sulfate and organic carbon) were considered for $q_L = 18$ g kg^{-1}. Simulation results showed that considering different chemical compositions of aerosol particles leads to changes in accumulated surface precipitation amount for a given CCN concentration, but the increasing trend of accumulated surface precipitation amount with CCN concentration is still observed (not shown).

In Eq. (2), the specified diabatic forcing weakens linearly with time after the initiation of surface precipitation and is absent some time τ after the onset of surface precipitation. Numerical experiments were performed with larger values of τ (60 and 90 min) for $q_L = 18$ g kg^{-1}. The accumulated surface precipitation amount as a function of CCN concentration in both the experiments is similar to that for $q_L = 18$ g kg^{-1} in Fig. 15 (not shown).

4. Summary and conclusions

In this study, the impacts of urban aerosols on clouds and precipitation were examined by performing a series of experiments with various aerosol concentrations and basic-state moisture profiles using a spectral microphysics cloud model. The urban heat island and urban air pollution are taken into account by setting that there is low-level heating in the urban area and that the aerosol concentration in the urban area is higher than that in the surrounding rural area. The urban heat island dynamically induces a low-level updraft on the downwind side

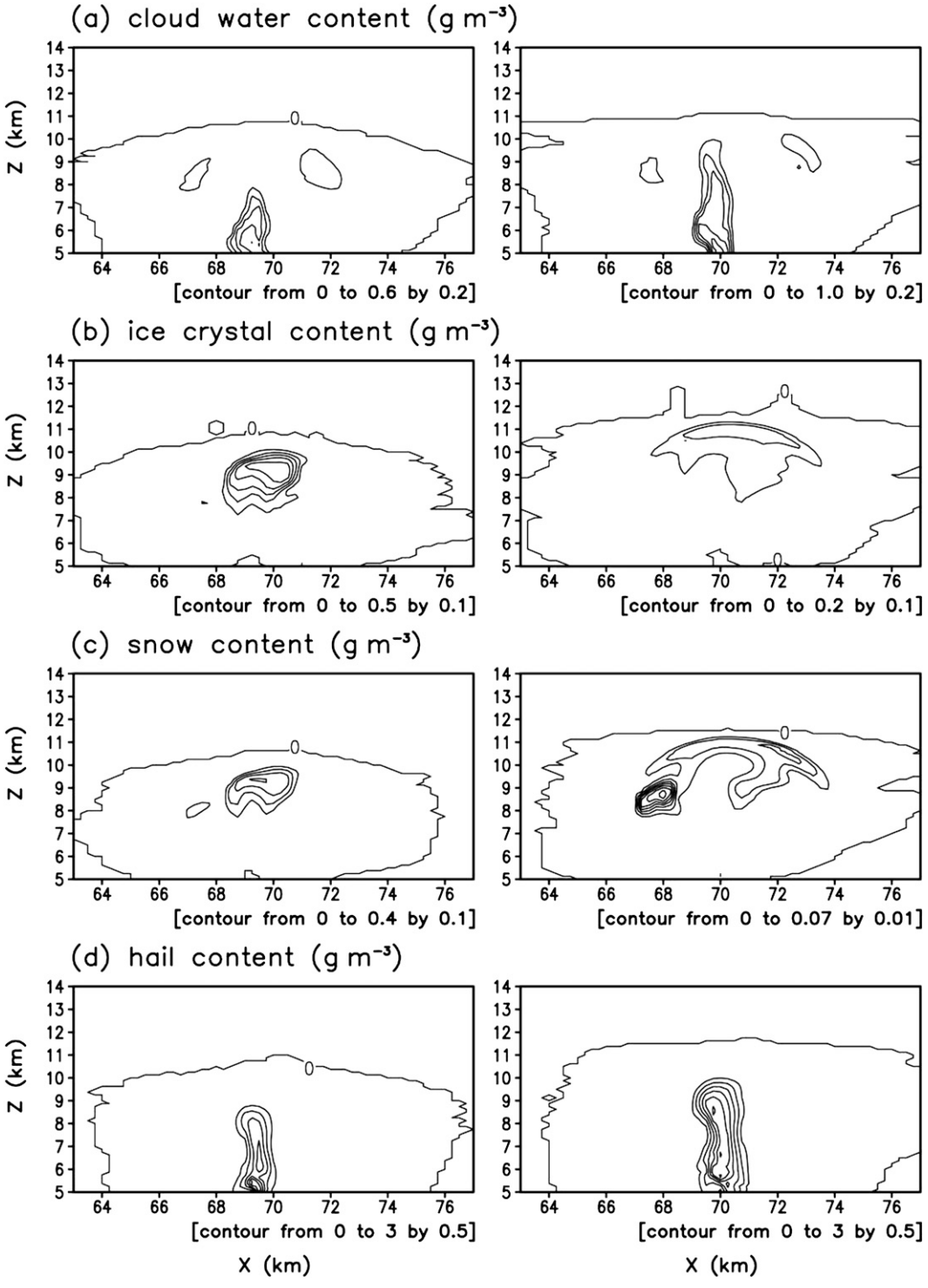

FIG. 10. The (a) cloud water, (b) ice crystal, (c) snow, and (d) hail content fields above $z = 5$ km near the time of maximum updraft in the deep convective cloud (i.e., at $t = 250$ min) in the cases of $q_L = 18$ g kg^{-1} and N_{CCN} = (left) 500 and (right) 4000 cm^{-3}. Note that different contour intervals are used in (c) between the low and high CCN concentration cases to well represent the configuration of each snow content field. The urban center is located at $x = 50$ km.

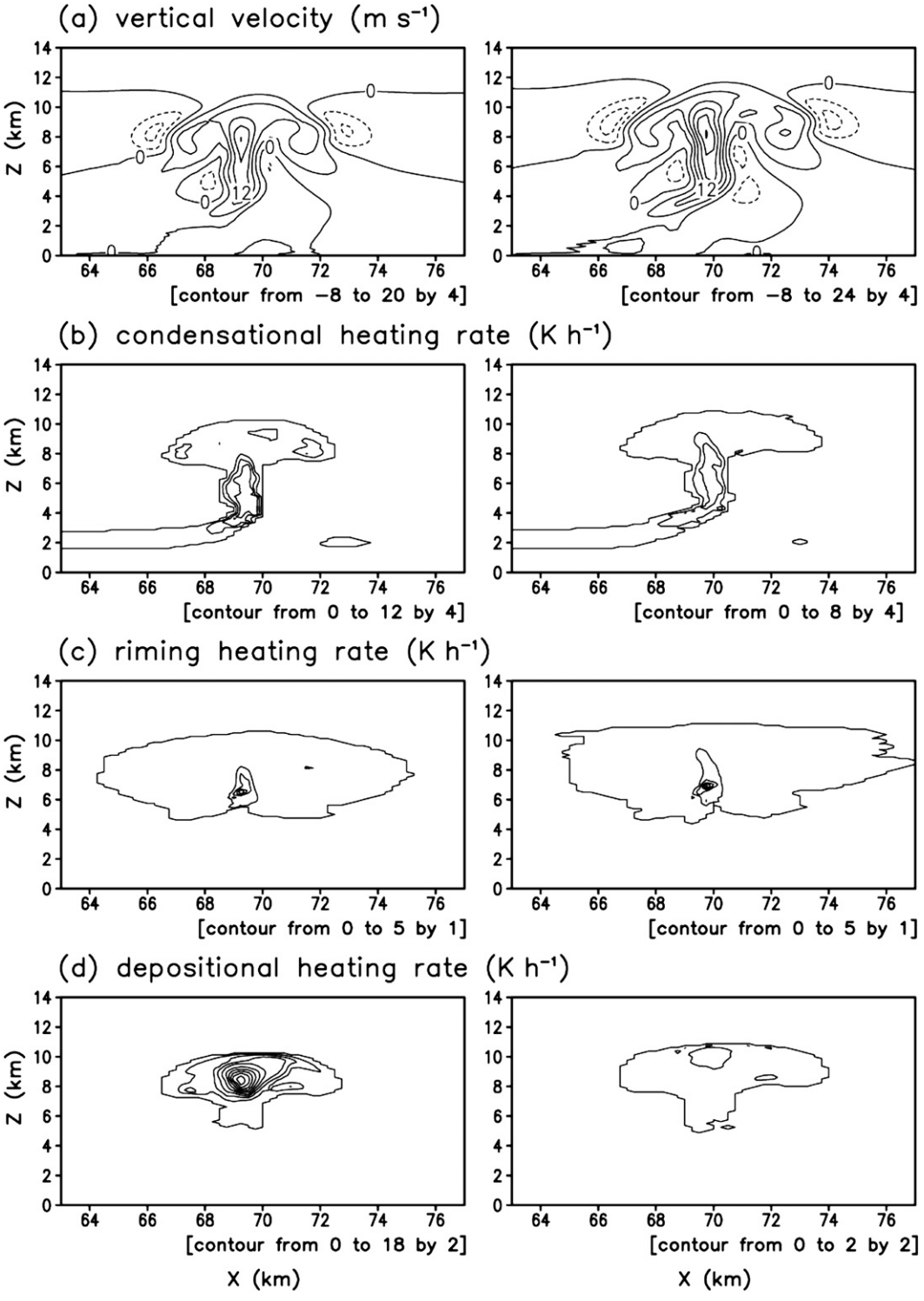

FIG. 11. (a) The vertical velocity field and the (b) condensational, (c) riming, and (d) depositional heating rate fields at $t = 250$ min in the cases of $q_L = 18$ g kg^{-1} and $N_{CCN} =$ (left) 500 and (right) 4000 cm^{-3}. The urban center is located at $x = 50$ km.

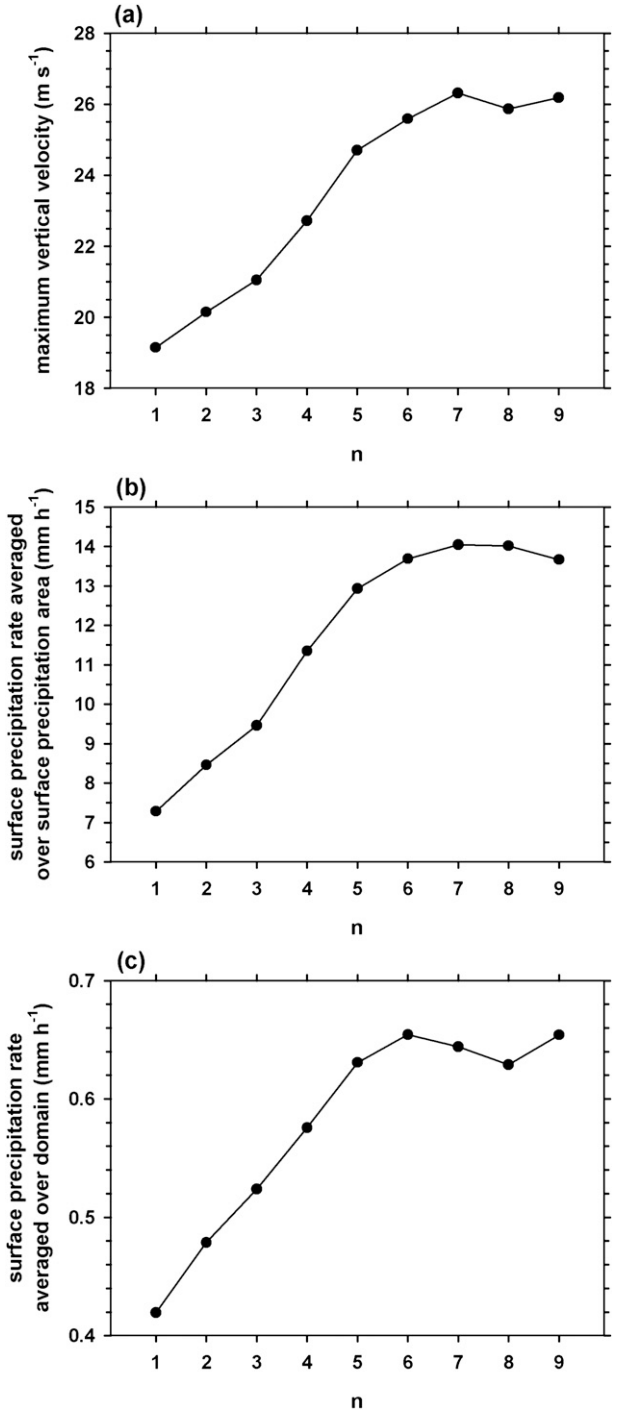

FIG. 12. (a) The maximum vertical velocity in the deep convective cloud and the corresponding local maximum precipitation rate averaged over the (b) surface precipitation area and (c) domain as a function of n for $q_L = 18$ g kg^{-1}.

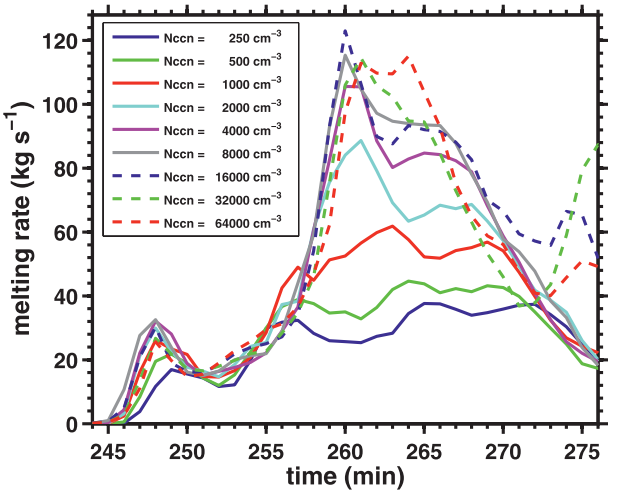

FIG. 13. The time evolution of the melting rate of the deep convective cloud system with various CCN concentrations for $q_L = 18$ g kg^{-1}.

not far from the urban center. This low-level updraft initiates a low-level cloud. The intensity of the low-level downdraft that develops in the low-level cloud increases with increasing aerosol concentration. This is because at higher aerosol concentrations, both the smaller drop size and the increased mass available for evaporation increase evaporative cooling in the downdraft region. In addition, the increased vertical advection of dry air resulting from stronger downdraft leads to a further increase in the intensity of the downdraft. The increase in aerosol concentration also results in a delayed onset of surface precipitation produced by the low-level cloud because of late raindrop formation, even though there is no discernible relation between aerosol concentration and the time required from the first raindrop formation to the initiation of surface precipitation. These aerosol impacts on the low-level cloud and precipitation are summarized in a schematic diagram (Fig. 16).

After the low-level cloud produces the light precipitation, a weak updraft cell separated from the low-level updraft initiates a deep convective cloud downwind of the low-level cloud. At higher aerosol concentrations where a higher number of smaller cloud drops with low collision efficiency result in an enhanced condensation process in the strong updraft region, the release of increased amount of latent heat causes invigoration of the well-organized deep convective cloud. After ice microphysical processes become active, not only the condensation process but also the riming process of the collisions of ice crystal and snow with supercooled water drops to produce graupel/hail are enhanced at higher levels with increasing aerosol concentration. This is because at higher aerosol concentrations, high liquid water content (LWC) exists at higher levels because of the low collision efficiency of smaller cloud drops and the resulting stronger updraft. On the other hand, lower supersaturation with respect to ice suppresses the deposition process. The melting of a larger

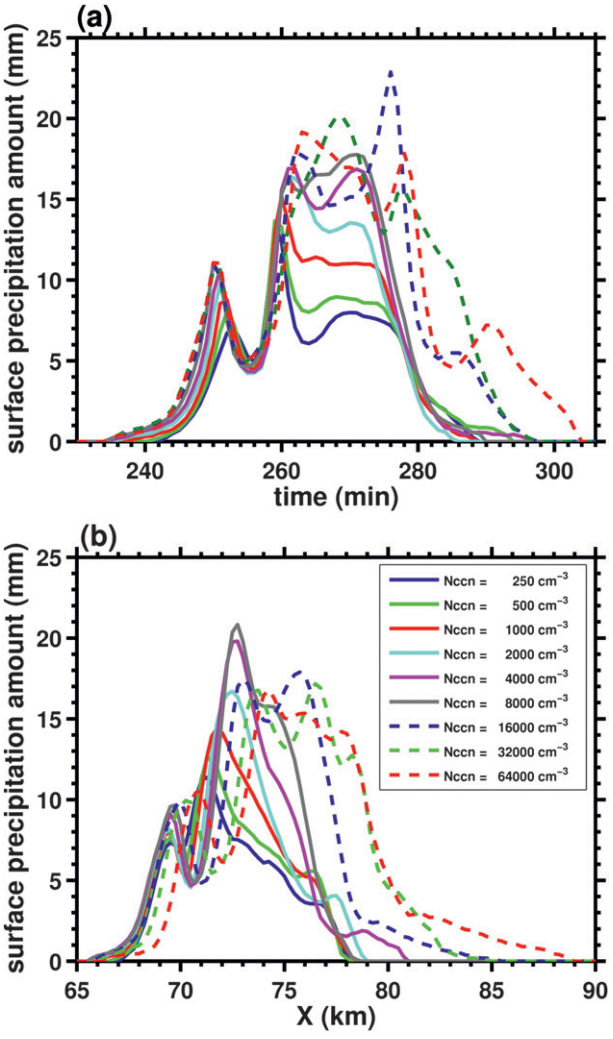

FIG. 14. The (a) time evolution and (b) horizontal distribution of surface precipitation amount summed over the area where the surface precipitation rate resulting from the deep convective cloud system is larger than 5 mm h^{-1} with various CCN concentrations for $q_L = 18$ g kg^{-1}. The urban center is located at $x = 50$ km.

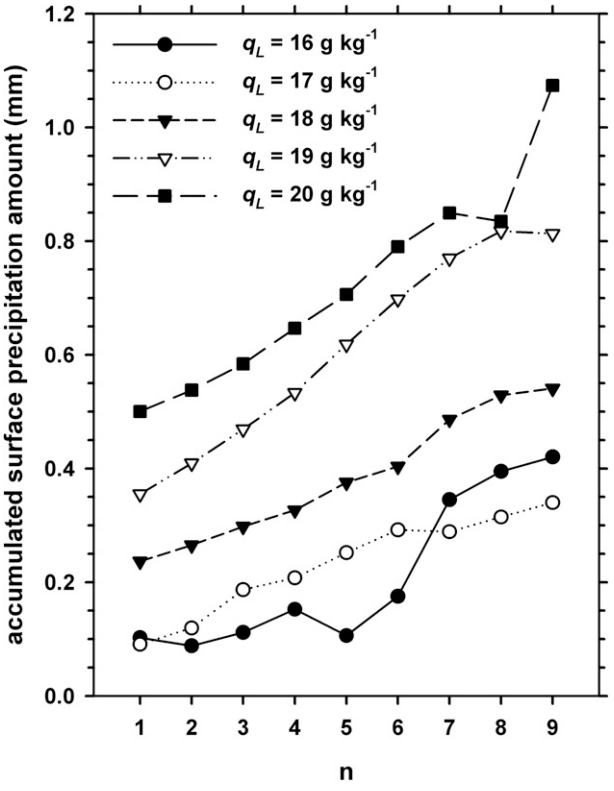

FIG. 15. The accumulated surface precipitation amount averaged over the domain as a function of n in the cases of $q_L = 16, 17, 18, 19$, and 20 g kg^{-1}.

amount of hail produced by the enhanced riming process leads to precipitation enhancement downwind of the urban area with increasing aerosol concentration under all environmental moisture conditions considered. These aerosol impacts on the deep convective cloud and precipitation are summarized in a schematic diagram (Fig. 17).

This study investigated the impacts of increased urban aerosols on clouds and precipitation, and the results suggest that the amount of downwind precipitation induced by an urban heat island can change significantly depending on the aerosol concentration in an urban area. However, in this study, another important effect of aerosols, the radiative effect of aerosols, was not considered. Aerosols stabilize the lower atmosphere by absorbing and scattering solar radiation (Rosenfeld et al. 2008), and the low-level stability is known to be an important factor in determining the intensities of circulation induced by an urban heat island and the resulting convective activity

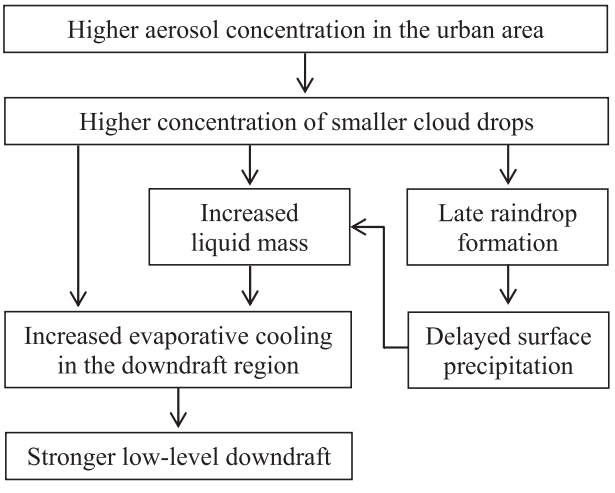

FIG. 16. Schematic diagram that shows how increased aerosol concentration in the urban area affects the low-level cloud.

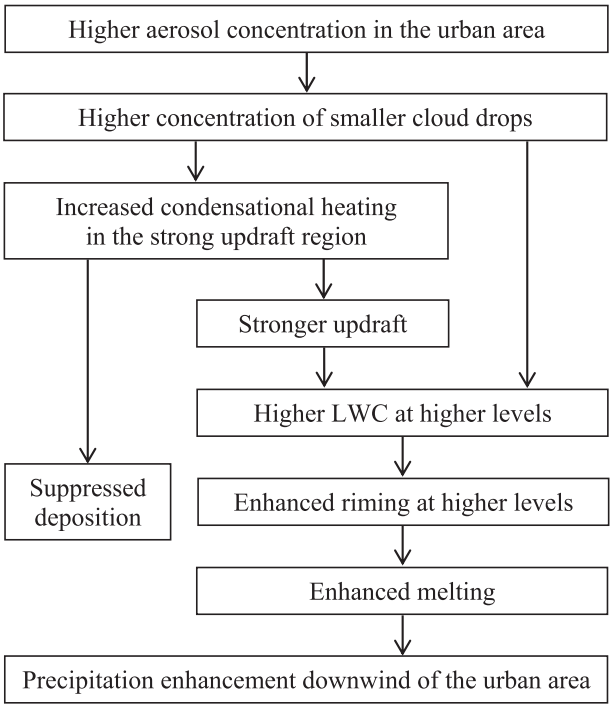

FIG. 17. Schematic diagram that shows how increased aerosol concentration in the urban area affects the deep convective cloud.

(Baik et al. 2007). The present study will be extended to investigate the microphysical and radiative effects of urban aerosols on clouds and precipitation using a cloud model including radiative processes.

Acknowledgments. The authors are very grateful to two anonymous reviewers for providing valuable comments on this work. This work was funded by the Korea Meteorological Administration Research and Development Program under Grant CATER 2006-2202. The third author was supported by the Israel Science Foundation (Grant 140/07). The authors would like to acknowledge the support from KISTI supercomputing center through the strategic support program for the supercomputing application research.

REFERENCES

Andreae, M. O., 2009: Correlation between cloud condensation nuclei concentration and aerosol optical thickness in remote and polluted regions. *Atmos. Chem. Phys.,* **9,** 543–556.

——, D. Rosenfeld, P. Artaxo, A. A. Costa, G. P. Frank, K. M. Longo, and M. A. F. Silva-Dias, 2004: Smoking rain clouds over the Amazon. *Science,* **303,** 1337–1342.

Baik, J.-J., Y.-H. Kim, and H.-Y. Chun, 2001: Dry and moist convection forced by an urban heat island. *J. Appl. Meteor.,* **40,** 1462–1475.

——, ——, J.-J. Kim, and J.-Y. Han, 2007: Effects of boundary-layer stability on urban heat island-induced circulation. *Theor. Appl. Climatol.,* **89,** 73–81.

Bell, T. L., D. Rosenfeld, K.-M. Kim, J.-M. Yoo, M.-I. Lee, and M. Hahnenberger, 2008: Midweek increase in U.S. summer rain and storm heights suggests air pollution invigorates rainstorms. *J. Geophys. Res.,* **113,** D02209, doi:10.1029/2007JD008623.

Bornstein, R., and Q. Lin, 2000: Urban heat islands and summertime convective thunderstorms in Atlanta: Three case studies. *Atmos. Environ.,* **34,** 507–516.

Changnon, S. A., R. T. Shealy, and R. W. Scott, 1991: Precipitation changes in fall, winter, and spring caused by St. Louis. *J. Appl. Meteor.,* **30,** 126–134.

Han, J.-Y., and J.-J. Baik, 2008: A theoretical and numerical study of urban heat island–induced circulation and convection. *J. Atmos. Sci.,* **65,** 1859–1877.

Inoue, T., and F. Kimura, 2004: Urban effects on low-level clouds around the Tokyo metropolitan area on clear summer days. *Geophys. Res. Lett.,* **31,** L05103, doi:10.1029/2003GL018908.

Jauregui, E., and E. Romales, 1996: Urban effects on convective precipitation in Mexico City. *Atmos. Environ.,* **30,** 3383–3389.

Kar, S. K., Y.-A. Liou, and K.-J. Ha, 2009: Aerosol effects on the enhancement of cloud-to-ground lightning over major urban areas of South Korea. *Atmos. Environ.,* **92,** 80–87.

Khain, A. P., 2009: Notes on state-of-the-art investigations of aerosol effects on precipitation: A critical review. *Environ. Res. Lett.,* **4,** 015004, doi:10.1088/1748-9326/4/1/015004.

——, and I. Sednev, 1996: Simulation of precipitation formation in the eastern Mediterranean coastal zone using a spectral microphysics cloud ensemble model. *Atmos. Res.,* **43,** 77–110.

——, A. Pokrovsky, M. Pinsky, A. Seifert, and V. Phillips, 2004: Simulation of effects of atmospheric aerosols on deep turbulent convective clouds using a spectral microphysics mixed-phase cumulus cloud model. Part I: Model description and possible applications. *J. Atmos. Sci.,* **61,** 2963–2982.

——, D. Rosenfeld, and A. Pokrovsky, 2005: Aerosol impact on the dynamics and microphysics of deep convective clouds. *Quart. J. Roy. Meteor. Soc.,* **131,** 2639–2663.

——, N. BenMoshe, and A. Pokrovsky, 2008: Factors determining the impact of aerosols on surface precipitation from clouds: An attempt at classification. *J. Atmos. Sci.,* **65,** 1721–1748.

——, D. Rosenfeld, A. Pokrovsky, U. Blahak, and A. Ryzhkov, 2011: The role of CCN in precipitation and hail in a mid-latitude storm as seen in simulations using a spectral (bin) microphysics model in a 2D dynamic frame. *Atmos. Res.,* **99,** 129–146.

Köhler, H., 1936: The nucleus in and the growth of hygroscopic droplets. *Trans. Faraday Soc.,* **32,** 1152–1161.

Koren, I., Y. J. Kaufman, D. Rosenfeld, L. A. Remer, and Y. Rudich, 2005: Aerosol invigoration and restructuring of Atlantic convective clouds. *Geophys. Res. Lett.,* **32,** L14828, doi:10.1029/2005GL023187.

Lacke, M. C., T. L. Mote, and J. M. Shepherd, 2009: Aerosols and associated precipitation patterns in Atlanta. *Atmos. Environ.,* **43,** 4359–4373.

Lee, S. S., L. J. Donner, V. T. J. Phillips, and Y. Ming, 2008: The dependence of aerosol effects on clouds and precipitation on cloud-system organization, shear and stability. *J. Geophys. Res.,* **113,** D16202, doi:10.1029/2007JD009224.

Lin, J. C., T. Matsui, R. A. Pielke Sr., and C. Kummerow, 2006: Effects of biomass-burning-derived aerosols on precipitation and clouds in the Amazon Basin: A satellite-based empirical study. *J. Geophys. Res.,* **111,** D19204, doi:10.1029/2005JD006884.

Lynn, B., A. P. Khain, D. Rosenfeld, and W. L. Woodley, 2007: Effects of aerosols on precipitation from orographic clouds. *J. Geophys. Res.,* **112,** D10225, doi:10.1029/2006JD007537.

Mote, T. L., M. C. Lacke, and J. M. Shepherd, 2007: Radar signatures of the urban effect on precipitation distribution: A case study for Atlanta, Georgia. *Geophys. Res. Lett.,* **34,** L20710, doi:10.1029/2007GL031903.

Naccarato, K. P., O. Pinto Jr., and I. R. C. A. Pinto, 2003: Evidence of thermal and aerosol effects on the cloud-to-ground lightning density and polarity over large urban areas of Southeastern Brazil. *Geophys. Res. Lett.,* **30,** 1674, doi:10.1029/2003GL017496.

Noppel, H., U. Blahak, A. Seifert, and K. D. Beheng, 2010: Simulations of a hailstorm and the impact of CCN using an advanced two-moment cloud microphysical scheme. *Atmos. Res.,* **96,** 286–301.

Ntelekos, A. A., J. A. Smith, L. Donner, J. D. Fast, W. I. Gustafson Jr., E. G. Chapman, and W. F. Krajewski, 2009: The effects of aerosols on intense convective precipitation in the northeastern United States. *Quart. J. Roy. Meteor. Soc.,* **135,** 1367–1391.

Oke, T. R., 1987: *Boundary Layer Climates*. 2nd ed. Routledge, 435 pp.

Orville, R. E., and Coauthors, 2001: Enhancement of cloud-to-ground lightning over Houston, Texas. *Geophys. Res. Lett.,* **28,** 2597–2600.

Pinsky, M., and A. P. Khain, 1998: Some effects of cloud turbulence on water-ice and ice-ice collisions. *Atmos. Res.,* **47-48,** 69–86.

——, ——, and M. Shapiro, 1999: Collisions of small drops in a turbulent flow. Part I: Collision efficiency. Problem formulation and preliminary results. *J. Atmos. Sci.,* **56,** 2585–2600.

——, ——, and ——, 2000: Stochastic effects of cloud droplet hydrodynamic interaction in a turbulent flow. *Atmos. Res.,* **53,** 131–169.

Pruppacher, H. R., and J. D. Klett, 1997: *Microphysics of Clouds and Precipitation*. Kluwer Academic, 954 pp.

Rose, L. S., J. A. Stallins, and M. L. Bentley, 2008: Concurrent cloud-to-ground lightning and precipitation enhancement in the Atlanta, Georgia (United States), urban region. *Earth Interactions,* **12.** [Available online at http://EarthInteractions.org.]

Rosenfeld, D., 2000: Suppression of rain and snow by urban and industrial air pollution. *Science,* **287,** 1793–1796.

——, U. Lohmann, G. B. Raga, C. D. O'Dowd, M. Kulmala, S. Fuzzi, A. Reissell, and M. O. Andreae, 2008: Flood or drought: How do aerosols affect precipitation? *Science,* **321,** 1309–1313.

Rozoff, C. M., W. R. Cotton, and J. O. Adegoke, 2003: Simulation of St. Louis, Missouri, land use impacts on thunderstorms. *J. Appl. Meteor.,* **42,** 716–738.

Seifert, A., and K. D. Beheng, 2006: A two-moment cloud microphysics parameterization for mixed-phase clouds. Part 2: Maritime vs. continental deep convective storms. *Meteor. Atmos. Phys.,* **92,** 67–82.

Shepherd, J. M., 2005: A review of current investigations of urban-induced rainfall and recommendations for the future. *Earth Interactions,* **9.** [Available online at http://EarthInteractions.org.]

——, H. Pierce, and A. J. Negri, 2002: Rainfall modification by major urban areas: Observations from spaceborne rain radar on the TRMM satellite. *J. Appl. Meteor.,* **41,** 689–701.

Tao, W.-K., X. Li, A. P. Khain, T. Matsui, S. Lang, and J. Simpson, 2007: Role of atmospheric aerosol concentration on deep convective precipitation: Cloud-resolving model simulations. *J. Geophys. Res.,* **112,** D24S18, doi:10.1029/2007JD008728.

van den Heever, S. C., and W. R. Cotton, 2007: Urban aerosol impacts on downwind convective storms. *J. Appl. Meteor. Climatol.,* **46,** 828–850.

Westcott, N. E., 1995: Summertime cloud-to-ground lightning activity around major Midwestern urban areas. *J. Appl. Meteor.,* **34,** 1633–1642.